Journal of Materials Science: Materials in Electronics (2020) 31:6511–6524
https://doi.org/10.1007/s10854-020-03241-w

REVIEW

Preparation and characterization of $MnTiO_3$, $FeTiO_3$, and $CoTiO_3$ nanoparticles and investigation various applications: a review

Sajad Ghaemifar[1] · Mahdi Rahimi-Nasrabadi[2,3] · Saeid Pourmasud[4] · Mohammad Eghbali-Arani[4] · Mohesn Behpour[5] · Ali Sobhani-Nasab[6,7]

Received: 15 November 2019 / Accepted: 10 March 2020 / Published online: 20 March 2020

Abstract
The fabrication of nanoceramices and nanomaterials with desirable morphology, structure, and particle size is one of the most important fields in the nanoscience. In order to achieve this goal, the sol–gel method is one of the most applicable methods which allow us to attain desirable structures by changing some parameters. This review focuses on the synthesis of some $MTiO_3$ (M = transition metals) by different routs owing to the technological importance of this group of materials. It also investigates different properties of such materials including photocatalytic, dielectric, optical and electrocatalytic behaviors. The conventional titanates of $MnTiO_3$, $FeTiO_3$, and $CoTiO_3$ are introduced and furthermore, their syntheses have been clarified by proposing a related mechanism. The effects of reactants concentration, time and temperature reaction, surfactant, M^{2+} and Ti^{4+} sources, etc. on the particle size, morphology, and some properties of the obtained nanomaterials have been investigated. The size and morphology of the as-synthesized samples are studied by the X-ray diffraction, scanning electron microscopy and transmission electron microscopy images. The optical, magnetic, and photocatalytic properties of the $MTiO_3$ are studied as well.

1 Introduction

The ability of measurement, designing, and manipulation at molecular and supermolecular levels on a scale of about 1 to 100 nm in order to understand, create, and use material structures, systems, and devices with essentially novel properties and functions which are caused by their small structures is named "Nanotechnology". Investigation and production of nanomaterials are proliferating significantly. The small size of nanostructured devices and functionality of nanostructured materials led to this fact that every aspect of human life could be changed by this feature. This technology is used in various fields including semiconductors in computers, drug delivery, photocatalyst, sensor, anticancer, cardiac stents, etc. [1–16].

$MTiO_3$ are not only able to combine different ferroic properties (ferroelectricity, magnetism, and elasticity) but also their technological applications, particularly in the electronics industry led to an extensively scientific attention. Especially, materials with the type of ABO_3 are extensively scrutinized for technological purposes, for instance gas sensors, ferroelectric devices, as well as actuators. Scheme. 1 shows different applications for $MTiO_3$ nanostructures. Hence, new multiferroic materials are capable to synthesize based on the aforementioned class of compounds. Scheme 2 show structure of a perovskite with general chemical formula $MTiO_3$. A perovskite is any material with the same type of crystal structure as $MnTiO_3$, $FeTiO_3$ and $CoTiO_3$, known as the perovskite structure ($ATiO_3$).

✉ Mahdi Rahimi-Nasrabadi
rahiminasrabadi@gmail.com

✉ Ali Sobhani-Nasab
Ali.sobhaninasab@gmail.com

1 School of Metallurgy and Materials Engineering, University of Tehran, Tehran, Iran

2 Nanobiotechnology Research Center, Baqiyatallah University of Medical Sciences, Tehran, Iran

3 Faculty of Pharmacy, Baqiyatallah University of Medical Sciences, Tehran, Iran

4 Department of Physics, University of Kashan, Kashan, Iran

5 Institute of Nano Science and Nano Technology, University of Kashan, P.O. Box 87317-51167, Kashan, Islamic Republic of Iran

6 Social Determinants of Health (SDH) Research Center, Kashan University of Medical Sciences, Kashan, Iran

7 Core Research Lab, Kashan University of Medical Sciences, Kashan, Iran

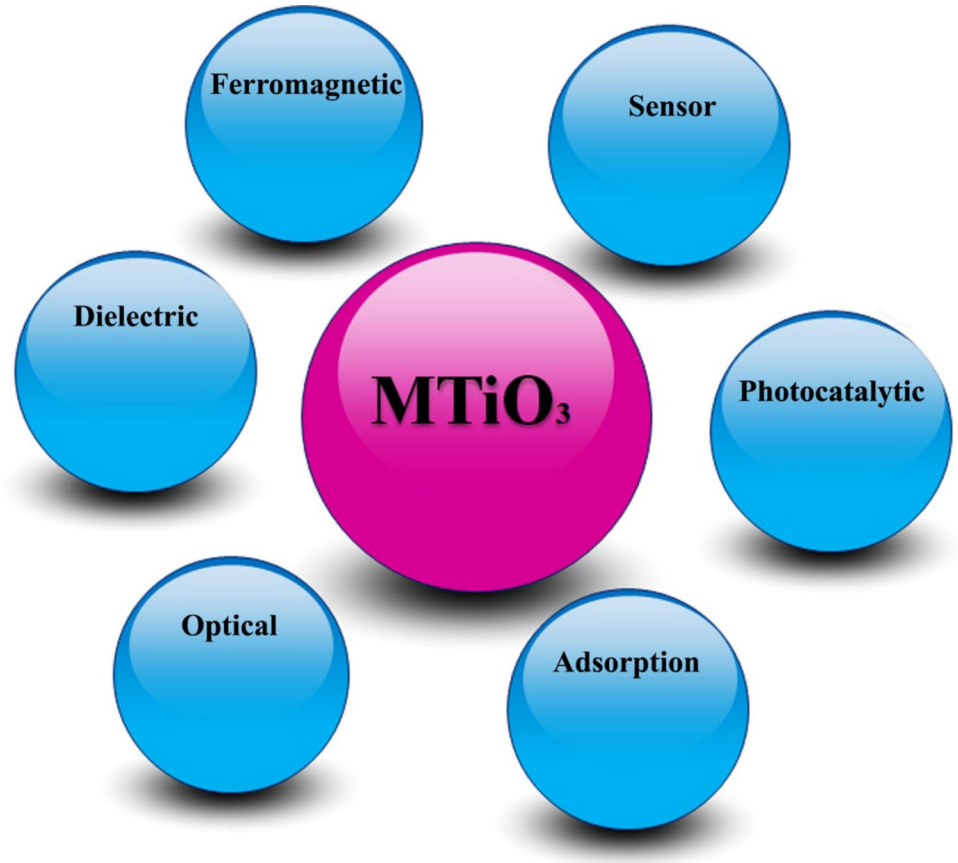

Scheme 1 Schematic different applications for the synthesis of $MnTiO_3$

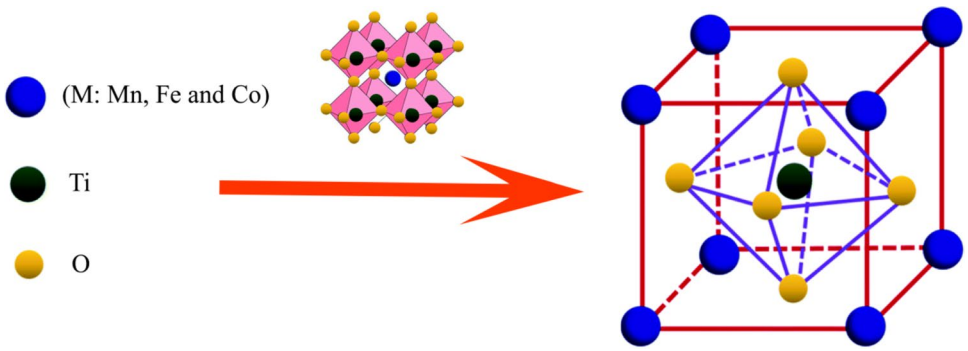

Scheme 2 Schematic of a perovskite with general chemical formula $MTiO_3$. The yellow spheres are oxygens atoms, the blak spheres are Ti atoms (a smaller metal cation), and the blue spheres are the M (Mn, Fe and Co) atoms (a larger metal cation) (Color figure online)

The traditional methods of synthesis material are also the base of many preparation methods for nanoscaled structures. However, new technologies have many advantages which can be utilized in order to fabricate nanoscaled structures. The combination of a number of different methods is still common to develop novel technologies. Different methods such as zeolite encapsulation, thermal decomposition, co-precipitation, hydrothermal, sol–gel, ultrasonic irradiation, microwave and irradiation have been used to fabricate nanostructures [17–30]. Scheme 3 shows different methods for the synthesis of $MTiO_3$ nanostructures.

Sol–gel is a well-known and important preparation process in order to fabricate the transition metal titanate nanostructures. This method provides a resourceful approach to synthesize inorganic polymer and organic/inorganic hybrid materials. It has been reported that the use of sol–gel method has been started at the mid-1800s. The Schott Glass Company (Jena, Germany) used this technology one century later. Due to the fact that sol–gel process is able to perform under extraordinary mild conditions, it can be utilized in order to achieve products with different shapes, sizes, morphology, and formats such as fibers, films, and monosized and monoliths particles. Sol–gel method has widely applications in development of new materials which are used in membranes, fibers, optical gain media, photochromic and nonlinear applications, chemical sensors, solid state

Scheme 3 Schematic different chemical methods for the synthesis of $MnTiO_3$

electrochemical devices, catalysis, in diverse ranges of scientific and engineering fields, such as electronic industry, nuclear field and ceramic industry. The sol–gel process can be defined by following steps: (1) hydrolysis, (2) condensation, and (3) thermal decomposition of metal alkoxides or metal precursors in solution. In this process, in the beginning a stable solution with all necessary reagents which is referred to the sol is formed by the metal alkoxides or precursors. Afterwards, the hydrolysis and the condensation stages are performed on the sol in order to form a networked structure (gel), which led to a significant increase in the viscosity. In order to control the kinetics of the reactions, alcohol, water, acid or base can be used. For obtaining the desirable particle size, changing in precursor concentration, temperature and pH values can be helpful. For enabling the formation of a solid mass, an aging step is required which is essentially after the gel formation. The aging step involves the expulsion of solvent, Ostwald ripening, and phase transformation which this step may take up to [31–36].

2 $MnTiO_3$

Among all titanium-based oxides, $MnTiO_3$ is an attractive material due to its great properties. For instance, the strong absorption in the visible region led to the various applications such as photocatalysis and solar energy [37]. In other words, the magnetic and photoelctrochemical properties of manganese titanate are suitable for related aforementioned devices [38, 39]. Furthermore, it has been reported that it can be utilized in the humidity sensors [40]. Manganese titanate has been prepared by different methods such as chelating agent assisted precipitation approach [41], and sol–gel hydrothermal process [37]. The common reported structure of $MnTiO_3$ which adopts after synthesizing is ilmenite structure in which Mn^{2+} and Ti^{2+} layers alternate along the c-axis of the lattice in the hexagonal setting [41]. However, other structures such as perovskite have been reported [42]. The conventional methods of synthesizing $MnTiO_3$ powder perform at very high temperatures which have many disadvantages as a consequence [43]. Hence, synthesizing $MnTiO_3$ powder via a low temperature route has been established in many studies [44]. The impurity of the final product and low surface area of $MnTiO_3$ are some probable challenges [45]. Kharkwal et al. [41] used oxine (8-hydroxyquinoline) as a chelate agent in order to synthesis the high surface area $MnTiO_3$ powders at low temperatures. In this method, Ti metal powder was added to the solution of $MnCl_2{\cdot}4H_2O$ with an equal molar ratio under constant stirring at 70 °C. By the aid of ammonia solution, the pH increased up to 10 and as a result, a brown colored precipitate appeared. Afterward, the filtered precipitate was washed with aqueous ammonia solution and water. The efficiency of complexation by oxine was proved by EDS analysis of the precursor which demonstrated the presence of the both metals in equal ratio. The TG/DTA analysis showed that the major weight loss took place in a single step among 380 °C and 580 °C. The presence of bonded carbonate group was revealed by FT-IR spectrum of the brown solid. Furthermore, the mentioned carbonate group showed bands at 1058 cm^{-1}, 1169 cm^{-1}, 1464 cm^{-1}, 1578 cm^{-1}, and 1746 cm^{-1}, respectively. It has been reported that at 600 °C the formation of $MnTiO_3$ is occurred in 6 h [44]. Hence, in this investigation the decomposition of the precursors was performed at 600 °C for 12 h which led to a final product with black color. The X-ray diffraction (XRD) results indicated that pure pyrophanite $MnTiO_3$ has formed and the observed d values were in compliance with the JCPDS File No. 29-0902. Moreover, the calculated lattice parameters were $a = 5.140$ Å and $c = 14.30$ Å. The BET method has been performed in order to measure the surface area of $MnTiO_3$ and owing to the evolution of massive gas through the thermal decomposition, the result of the measurement was 140 m^2/g. The transmission electron microscopy (TEM) images showed nano bars like morphology of $MnTiO_3$ with an average diameter of 20 nm. Strong absorption had been observed for black $MnTiO_3$ in the visible region which start from 320 nm and λ_{max} is occurred at 620 nm. The charge transfer from O^{2-} to Ti^{4+} is the cuase of the wide absorption around 320 [45]. The absorption bands in the visible region were attributed to the $^6A_{1g}$ to $^4A_{1g}$ and $^6A_{1g}$ to $^6T_{1g}$ crystal field transition of octahedral Mn^{2+} site. As mentioned before and stated in

many studies [37] manganese titanate is one of the best candidates to be used in a solar energy system owing to its strong absorption in the visible wavelength region.

Bae et al. [46] investigated the effect of $MnTiO_3$ surface treatment on the performance of dye-sensitized solar cells (DSSCs). DSSCs based on nanoporous electrodes (commonly TiO_2) have widely inspired attention from scientific as well as technological viewpoint, due to their low cost, less toxic manufacturing process, and remarkable efficiencies [47]. Even though, charge recombination among other problems is the main challenge which leads to a significant degradation in the efficiency of DSSCs. Moreover, this problem is more to come in nanoporous TiO_2 electrode [48, 49]. Many surface treatments such as using metal oxides were performed to suppress the recombination and consequently enhance cell performance [50, 51]. It has been stated that the surface pH and the conduction band edge of $MnTiO_3$ are higher than those of TiO_2 [52]. Hence, the recombination will be reduced and more dye molecules can be absorbed in the basic pH at the electrode surface. In this study [46], nanoporous TiO_2 films were deposited onto transparent conducting glass substrates, and then calcined for 1 h at 500 °C. The $MnTiO_3$ treatment was accomplished afterward followed by sintering at 500 °C for 30 min in air. The XRD results indicated that the aforementioned surface treatment led to no significant shift in the diffraction peaks, which is attributed to the small amount of Mn. Moreover, the calculated average grain sizes of the bare and $MnTiO_3$-treated TiO_2 electrode were 26.6 and 28.2 nm, respectively which demonstrated that $MnTiO_3$ treated sample had a slightly larger size. Although XRF analysis confirmed the presence of Mn, no diffraction peaks of $MnTiO_3$ phases were seen in XRD results. FESEM micrographs demonstrated that $MnTiO_3$ -treated TiO_2 sample had smaller number of cracks than bare TiO_2 sample. Furthermore, it has been revealed that $MnTiO_3$ -treated TiO_2 particles are larger than the bare sample. According to the measured values which were obtained by root-mean square roughness measurement (86.2 nm for bare sample and 67.4 nm for $MnTiO_3$-treated sample), it can be inferred that the applied surface treatment led to a smoother surface through filling the cracks. TEM images showed that an amorphous $MnTiO_3$ layer (~ 2 nm thick) was formed on the treated TiO_2 sample. It has been reported that $MnTiO_3$ facilitates the connection of TiO_2 particles and as a consequence, it can help the photo-injected electrons to migrate to the TiO_2 conduction band and finally the reduction in the internal resistance was occurred [53]. The UV–Vis analysis demonstrated that the $MnTiO_3$-treated TiO_2 sample showed higher absorbance across the 450–800 nm wavelength region than the bare TiO_2 sample. The pH of the metal oxides plays a vital role in chemisorptions between sensitizer and semiconductor. It has been stated that if the pH of the oxide electrodes were more basic than the pH of the bare electrode, the dye molecules attach more effectively to the oxide electrodes. Furthermore, the calculated value of the point of zero charges for the $MnTiO_3$-treated TiO_2 and bare sample were 7.83 and 5.80, respectively [54]. Therefore, $MnTiO_3$ treatment led to higher pH_{ZPC} and facilitates the adhering of dye molecules to the electrode. It has been reported that about 25% higher cell efficiency had been achieved in DSSCs with the $MnTiO_3$-treated sample. This result is owing to the fact that according to the I-V characteristics of DSSCs fabricated with and without the $MnTiO_3$ treatment, higher short circuit current (15.7 mA/cm^2) and higher open-circuit voltage (0.67 V) had been observed.

Decontamination of wastewater containing dyes is a crucial issue and also a global concern which has been the goal of many studies in the last few years [55]. $MnTiO_3$ is one of the most important photocatalysts which can be utilized to overcome this environmental challenge. He et al. [56] studied the photodegradation of aqueous methyl orange on $MnTiO_3$ powder at different initial pHs. In this study, a citric-sol–gel method has been performed in order to synthesize the $MnTiO_3$ powder as a catalyst. Manganese chlorite tetrahydrate, acetic acid, and titanium propoxide were used as the precursors. TG/DSC analysis showed that the only exothermic peak appeared at 576.8 °C which corresponds to the crystallization of $MnTiO_3$. The peak temperature was near the value reported recently [40] and it has been stated that the calcinations temperature was 700 °C which was also selected in this study. XRD patterns indicated that rhombohedral pyrophanite $MnTiO_3$ was the only detected phase with JCPDS File No. 29–0902. The calculated lattice parameters were $a = b = 5.1391$ Å, and $c = 14.2988$ Å. Furthermore, the calculated average particle size at $2\theta = 32.079°$ was 43.7 nm. The scanning electron microscopy (SEM) images demonstrated a granular morphology for $MnTiO_3$ powder with an average particle size of approximately 80 nm. The UV–visible analysis showed that the absorption edge of the $MnTiO_3$ powder is in the visible light region at ~ 850 nm, which corresponds to band gap energy of 1.46 eV. However, this value for the bulk $MnTiO_3$ is 1.5 eV which is due to the quantum size effect of the powder. It has been revealed that low initial solution pH led to more efficiency in photodegradation of aqueous methyl orange on $MnTiO_3$. Moreover, H_2O_2 enhances the decolorization kinetic of the aqueous methyl orange solution on $MnTiO_3$. Therefore, $MnTiO_3$ powder is an extraordinary photocatalyst which can be utilized for decontamination. Table 1 shows a summary of the several of synthesis methods and precursors applied in the preparation of $MnTiO_3$ nanoparticles.

Among the different synthesis methods mentioned for $MnTiO_3$, sol gel synthesis is one of the best methods. This method synthesizes better quality nanoparticles with finer size and more uniform size distribution. Also this method allows better control of particle size and morphology by

Table 1 Selected approaches for synthesis of $MnTiO_3$ nanopaerticles and their applications

Synthesis method	Band gap	Precursors	Average size (nm)	Property	Ref
Solid state	4.28	Manganese carbonate and titanium dioxide	3–10 nm	Dielectric	[57]
Sol–gel	2.9	$Mn(NO_3)_2{\cdot}H_2O$ and Titanium butoxide	12.17 nm	Photocatalytic	[58]
Solid state	–	MnO_2 and TiO_2	–	Magnetization ceramics	[59]
Hydrothermal	–	Manganese nitrate and $TiCl_4$	100 nm	Photocatalytic	[60]
Sol–gel	–	$Mn(CH_3COO)_2{\cdot}4H_2O$and $Ti[OCH(CH_3)_2]_4$	300–400 nm	–	[61]
Hydrothermal	–	$MnCl_2{\cdot}4H_2O$ and Titanium	Thickness 80	Photocatalytic	[62]
Oxidation	–	$MnCl_2{\cdot}4H_2O$ and Titanium dioxide	40–60 nm	Optical	[44]

selecting different precursors and modifying the synthesis conditions for example pH, temperature and other conditions.

3 $FeTiO_3$

$FeTiO_3$ is one of the most common minerals in the natural resources in the Earth crust. It has a Neel temperature of 55 K with rhombohedral structure (space group of $R\bar{3}$) [63]. $FeTiO_3$ has a fascinating broad band gap (2.58–2.9 eV) antiferromagnetic semiconductor which has various applications such as optoelectronics, spintronics, chemical catalysts, high temperature integrated circuits, and photocatalysts. [64–67]. Many methods have been utilized for synthesis of $FeTiO_3$ such as ball milling, chemical reduction techniques, sol–gel method, co-precipitation, hydrothermal reaction, microwave-assisted preparation, solid state reaction, ionic-liquid-assisted solution chemistry, etc. [66, 68–70]. Due to the disadvantages of the conventional methods such as solid state reaction owing to their high temperature, the interest in the sol–gel process is continuously increasing. The homogeneity, lower crystallization temperature, and finer crystallite size are some advantages of the sol–gel method.

Gambhire et al. studied the preparation of $FeTiO_3$ via sol–gel process combined with a surfactant-assisted template method [71]. For modification of the microstructure of the gels, the cationic surfactant cetyltrimethylammonium bromide (CTAB) has been used as a structure directing agent by mixing it in an alkoxide solution. Moreover, after producing the brown fluffy porous gels, it was calcined at various temperatures ranging 150–600 °C for 2 h in air. The XRD results demonstrated that no structure evolution occurred at the temperatures below 300 °C and crystallization begun at 500 °C. It is noteworthy to state that base on the XRD results calcination at 500 °C led to the formation of an anatase phase at $2\theta = 25.32°$, 48.06°, 55.09°, and 62.16° and a rutile phase at $2\theta = 27.44°$, 36.09°, 41.25°, and 44.05°. However, XRD patterns of calcination temperature at 600 °C revealed the formation of pure $FeTiO_3$ which has hexagonal crystal structure with JCPDS card no. 75-1207. The calculated lattice parameters and particle size were $a = 5.141$ Å, $c = 14.22$ Å, and $d = 25$nm, respectively. The TEM images showed that the particle morphology of the sample which calcined at 600 °C was nearly spherical with uniform size and the particle size distribution was in the range of 23–25 nm. Furthermore, FT-IR spectra, XPS, and TG/DSC analysis have been performed and it has been inferred that 600 °C is the temperature which the formation of $FeTiO_3$ was completed and this is in consistent with the XRD and TEM results.

Srinivas et al. investigated the synthesis and magnetic properties of nanocrystalline $FeTiO_3$ materials by a sol–gel auto-ignition method [72]. At first, ferric nitrate and $C_6H_8O_7$ were dissolved in distilled water which nominated as solution A. Afterward, C_3H_8O was dropped to the titanium isopropoxide and finally, acetic acid and methanol were added in order to obtain solution B. Solution B was added to solution A and ammonia solution was used to adjust the pH. The black gel was formed after increasing temperature to 200 °C. Moreover, the temperature increased to 380 °C which led to the start of the auto-ignition. Finally, the powders were annealed at 500 °C in air for 10 h. The XRD patterns of these powders showed some undesirable products such as TiO_2, Fe_2O_3, and Fe_3O_4 along with the presence of $FeTiO_3$. In order to solve this problem, the prepared material was pressed in the form of pellets accompanied by sealing in a quartz tube under a pressure of $\sim 10^{-5}$ mtorr and annealing for 10 h at 500 °C. The XRD pattern of the modified material showed that all impurities except small amount of TiO_2 were eliminated and the reflections are in consistent with JCPDS card no. 75-1211 (rhombohedral crystal structure with the space group of R3c). By means of alternating the concentrations of pH from 7 to 9, three different size distributions of nanoparticles were achieved which nominated S1, S2, and S3. The calculated lattice parameters are $a = 5.066$ Å and $c = 13.953$ Å for S1, $a = 5.122$ Å and $c = 13.788$ Å for S2, and $a = 5.123$ Å and $c = 13.881$ Å for S3. The average particle sizes for these samples are 20, 30, and 54 for S1, S2, and S3, respectively. In order to investigate the magnetic properties, the PPMS-VSM (QD) was used. Magnetization (M)

against temperature (T) was performed in zero-field-cooled (M_{ZFC}) and field-cooled (M_{FC}) modes in the temperature range from 2 to 300 K with the applied fields of 50 Oe and 1 kOe for all the samples. It had been revealed for S1 that the antiferromagnetic ordering takes place at about 55 K, and below 10 K, there is an abrupt jump in magnetization demonstrating the onset of the ferromagnetic order. It had been stated for S2 that the observed peak around 52 K is similar to the one observed for the S1 which shows antiferromagnetic-like ordering, and the concave curvature at 15 K is owing to competition among ferromagnetic and antiferromagnetic ordering. Furthermore, susceptibility versus temperature plots follows the Curie–Weiss law well above the peak temperature. According to this law and the fitting data, the effective magnetic moment values were calculated 4.62, 4.50, and 5.39 μ_B for S1, S2, and S3, respectively. It has been reported that by increasing the particle size, an increasing in the values of the effective magnetic moment had been occurred and also the magnetic moment value for S3 is close to that of bulk $FeTiO_3$ [73]. The plots of magnetization versus temperature of the S1 and S2 systems indicate weak ferromagnetism at the lowest temperature while S3 system indicates only antiferromagnetic order. Hence, it can be concluded that the disappearing of weak ferromagnetism begins by increasing in particle size. Furthermore, the observations of exchange bias in the mentioned samples suggest the presence of both ferromagnetic and antiferromagnetic orders which is owing to the mixed valence state of Fe due to uncompensated spins present on the surface. Table 2 shows a summary of the various synthesis method and precursors applied in the preparation of $FeTiO_3$ nanoparticles.

Therefore, considering reading different papers, $FeTiO_3$ nanoparticles, have various applications as both photocatalytists and electrocatalytists. Also, these nanostructures have magnetic properties. Investigation on, varying methods for preparation of $FeTiO_3$ nanostructures showed that the sol–gel method is a widespread one for the fabrication of such particles. Moreover, using this economical procedure, one can produce homogeneous $FeTiO_3$ nanoparticles with appropriate size distribution which is tailored for industry production.

4 $CoTiO_3$

One of the most well-known perovskite type titanates is $CoTiO_3$ which has numerous applications such as magnetic recorders, nano-pigment, gas sensors, Li-ion batteries, and catalysts.[85–91]. It is noteworthy to state that $CoTiO_3$ has a narrow band gap (~ 2.3 eV) which led to various applications. Considering its potential applications in different fields, many various methods have been utilized to synthesize $CoTiO_3$ such as combustion synthesis, solid state, wet chemical methods which involves, sol–gel and reflux, pechini method, precipitation and co-precipitation, and hydrothermal [45, 92–96].

Due to high temperature calcination in the aforementioned methods, many disadvantages (i.e., large particle size, impure phases, and agglomeration) may occur. Hence, sonochemical synthesis in which operation in ambient conditions is possible, is a suitable solution in order to overcome to mentioned challenges [97, 98]. Moghtada et al. [99] scrutinized the synthesis of cobalt titanate by using low temperature sonochemical methods. In this work, $TiCl_4$, $CoCl_2$, ethanol, anhydrous sodium hydroxide, and EDTA were used as precursors. FT-IR analysis indicated that synthesized nanocrystals are without any intermediate phase owing the fact that the characteristic bands of the carbonates (867, 1067, 1440 cm^{-1}) have not observed in this analysis spectrum. XRD results demonstrated that the crystal structure of $CoTiO_3$ is rhombohedral and the d-lines pattern is in consistent with JCPDS File No. 29–0516. The observed peaks at $2\theta = 26.68$, 31.39, 36.82, 44.84, 59.52, 62.43 and 68.58 correspond to the lattice planes of (211),

Table 2 Selected approaches for synthesis of $FeTiO_3$ nanopaerticles and their applications

Synthesis method	Band gap	Precursors	Average size (nm)	Property	Ref
Precipitate	–	$FeCl_2{\cdot}4H_2O$ and Titanium isoproxide	500 and 300 nm	Electrocatalytic	[74]
Solid state	2.8 eV	$Fe(NO_3)_3$ $9H_2O$ and TiO_2	60 nm	Ferromagnetic	[75]
Sol–gel	2.6 eV	Tetra-*n*-butyl ortho titanate and $Fe(NO_3)_2{\cdot}9H_2O$	30–50 nm	Photochemical	[76]
Sol–gel	–	TiO_2 and Fe_2O_3	40 µm	photocatalytic	[77]
Hydrothermal	2.6 eV	Ferric nitrate and Titanium-oxalate	20–100 nm	Photocatalytic	[78]
Precipitation	–	Tetrabutyl titanate and Ferriccitrate pentahydrate	100 nm	Battery	[79]
Hydrothermal	–	Titanium isopropoxide and $FeSO_4{\cdot}7H_2O$	300 nm	Sensor	[80]
Ball milling	–	Iron oxide and Titanium oxide	100 and 1000 µm	Corrosion	[81]
Ball milling	–	Iron oxide and Titanium oxide	50 nm	Corrosion	[82]
Hydrothermal	–	$FeCl_3{\cdot}6H_2O$ and titanium isopropoxide	–	Photocatalytic	[83]
Hydrothermal	–	$FeCl_2{\cdot}4H_2O$ and TiO_2	500 nm	Photocatalytic	[84]

(310), (311), (410), (510), (521) and (124), respectively. Moreover, the calculated average grain size of the synthesized product was 10.7 nm. Furthermore, XRD comparison of powders synthesized with and without the presence of EDTA was performed and it has been concluded that by the aid of preparation with EDTA well crystallized $CoTiO_3$ can be achieved. However, in absence of EDTA, impurities such as Co_2O_3, CoO, and Co_2TiO_4 exist. The FESEM images showed that uniform crystal size and homogeneous morphology in shape and dimension for cobalt titanate nanocrystals obtained with EDTA. On the other hand, the morphology of $CoTiO_3$ nanocrystals without EDTA was erratically agglomerated and the size range was 100 to 150 nm. Furthermore, morphologies of $CoTiO_3$ nanocrystals without EDTA were ellipsoid-like and spheroid-like while morphologies of $CoTiO_3$ nanocrystals with EDTA were spheroid-like. Due to high surface energy and large surface area of nanoparticles, agglomeration which is a common phenomenon in wet chemical synthesis methods had occurred in order to reduce their surface energy. Moreover, with the aid of these micrographs, it has been stated that the average particle size and the average agglomerate size are 50 and 80 nm, respectively. It is vivid that the grain size of the powders is in nanometer scale and is in consistent with the values calculated from XRD results. However, owing to this fact that the size obtained by the SEM is the particle size and that obtained by the XRD is grain size, the size of 50 nm is larger than the value (10.7 nm) achieved from XRD patterns. In order to evaluate the optical responses and determinate the band gap of the powder samples, the UV–Vis diffuse reflectance spectroscopy (DRS) was used. The optical characteristic of nano-pigments in both the UV and visible light ranges was indicated by the DRS spectrum of the powder sample. Based on the recent investigation which has been done by Agui and Mizumaki (100), three possible types of electronic transitions can occur in $CoTiO_3$: between Co: 3d to Ti: 3d, between O: 2p and Ti: 3d, and between Co: 3d and O: 2p. Owing to the crystal field splitting, two absorption peaks were observed in the DRS spectrum of $CaTiO_3$ around 580 and 620 nm [20]. The 3 d^8 band associated with Co^{2+} ion splits up into two sub-bands named the Co^{2+} to Ti^{4+} charge transfer (CT) bands and a wide absorption edge at smaller wavelength which shows the optical band gap ascribed to the O^{2-} to Ti^{4+} charge transfer interaction. The calculated band gap of the $CaTiO_3$ nanoparticles was calculated about 4.64 eV which was calculated from the reflection peak at 267 nm. $CaTiO_3$ nanoparticles show a high reflection peak at ~ 580 nm with an average reflection of 58%, which is higher than the previously reported value in the similar studies [19]. It can be inferred from the presence of an absorption in the range of 550–600 nm of the spectrum that the color of the synthesized nano-pigments is green. All in all, nanoparticles was formed immediately and then aggregated to form large particles. By means of ultrasonic irradiation, narrow size distribution was attained for the aggregated particles. The extensive use of dyes and their presence in the effluents of industries as a consequence led to this environmental concern that these dyes must be eliminated from wastewater which is a challenging issue due to their chemical stability [100–104]. Hetero-structured nanocomposite transition metal oxides are good candidates in order to degrade organic pollutants [105]. Habibi et al. [106] worked on the synthesis of $CoTiO_3$ nanocomposite by a modified sol–gel method wherein and $Co(NO_3)_2$ were used as precursors and $C_4H_{10}O_3$ as a stabilizer. Initially, the aforementioned precursors were dissolved in ethanol separately and stirred for 30 min. Afterward, by adding a mixture of glacial acetic acid and ethanol to first solution and mixture of diethylene glycol and ethanol to other solution, yellow and red solutions obtained, respectively. Then, red solution was added dropwise into the yellow sol and after stirring for 2 h and sol aging for 4 days, the gel was dried at 80 °C. Finally, the dried gel was calcinated at different temperatures for 4 h. In order to determine the crystalline performance and estimate the best calcination temperature, TG and DTG experiments were performed on a sample of $CoTiO_3$ which led to this result that weight loss phases were completed at 750 °C with peak temperatures of 107 and 345 °C. Moreover, results showed that there is no significant weight loss above 550 °C. Hence, 550 °C was the temperature for starting calcination step. The XRD results indicated that calcination at 650 °C was best temperature due to formation of pure crystalline phase of $CoTiO_3$ nano-powders while, calcination at 550 and 750 °C led to formation of mixtures of $CoTiO_3$ (66%)—Co_3O_4 (21%)—TiO_2(13%) and $CoTiO_3$ (89%)—TiO_2 (11%), respectively. Furthermore, the synthesized $CoTiO_3$ was coated on glass by means of Doctor Blade method in order to evaluate photocatalytic activity. The FESEM image of coated sample calcined at 650 °C demonstrated that thin film has nanosize uniform. Moreover, the average nanoparticle size is about 58 nm which confirmed by XRD results. In order to estimate band gap of $CoTiO_3$ calcined at 650 °C, UV–Vis DRS spectra carried out. Based on this analysis and by using the Tauk plot, the band gap for ilmenite type $CoTiO_3$ was 1.38 eV (898 nm) and 1.54 eV (805 nm) and by using the Kubelka–Munk plot the band gap was 1.59 eV (779 nm) and 2.10 eV (590 nm). Hence, the lowest energy of band gap 1.59 eV (779 nm) which is within the visible light range. Photocatalytic activity of hetero-structured $CoTiO_3$ nanocomposite photocatalyst was examined for degradation of Nile blue dye and the results indicated the complete degradation in 2.5 h of light irradiation. It has been concluded that this result is caused by the visible light harvesting ability, efficient separation of electron–hole pairs of the $CoTiO_3$ nanocomposite, and narrow band gap.

Many investigations have been done in order to show that $CoTiO_3$ nanoparticles are suitable gas sensor material for the reliable, rapid, and robust ethanol detection under the dynamic conditions of flex fuel exhaust [90, 107]. One of the most well-known methods for synthesizing nanomaterials is sol–gel process which has numerous advantages such as purity, high homogeneity, and high surface area due to the ability to control the structure of materials. Lu et. al [108]. worked on synthesizing of gas sensing $CoTiO_3$ nanoparticles by sol–gel methods using EDTA as the chelating agent. Many researchers showed that the chelating agent has a vital role in synthesizing of uncontaminated $CoTiO_3$ nanoparticles in the sol–gel method. In other words, sphere-shaped and rod-shaped $CoTiO_3$ nanoparticles have been obtained with citric acid and ethylene glycol as chelate agents, respectively [94, 109]. In the aforementioned method, EDTA was dissolved in $NH_3 \cdot H_2O$ firstly and $Co(NO_3)_2 \cdot 6H_2O$ was added subsequently. Afterward, $Ti(OC_4H_9)_4$ was added to the mixed solution. In order to adjust the pH in the range of 2.0–5.0, CH_3COOH was used. The obtained solution dried which a purple-colored gel obtained and finally, calcination was performed at the range of 400 to 800 °C for 2 h. According to the TG-DSC analysis results, it can be stated that the 500–700 °C was the calcination temperature range for$CoTiO_3$. In other words, based on this analysis, decomposition of the network structured polymer into metal oxides and synthesizing into cobalt titanate occurred at around 573 °C. Moreover, this result confirmed by XRD patterns of samples calcined at the range of 400 to 800 °C. XRD patterns indicated that only Co_3O_4 existed at 400 to 500 °C. At 600 °C, $CoTiO_3$ diffraction peaks had been seen along with Co_3O_4 and TiO_2 diffraction peaks which are impurities. The samples with calcination temperature 800 °C indicated a complex composition due to the synthesis of Co_2TiO_4. For evaluating the effect of precursor pH, XRD analysis performed on the powders synthesized from precursors with various pH values. At the range of 2.0–4.0 sharp and intense peaks were observed which demonstrate the presence of fine crystalline $CoTiO_3$. The regarding JCPDS file number is 77-1373 which corresponds to the rhombohedral phase. Increasing the pH from 5.0 to 6.0 led to decreasing the intensity of $CoTiO_3$ diffraction peaks and also TiO, TiO_2 diffraction peaks appeared in this range of pH. This result can be explained by this fact that the hydrolysis speed of butyl titanate is sluggish; however, the polycondensation can be improved in neutral media. In other words, much more $Ti(OR)_m(OH)_n$ link into each other in neutral sol, which led to increase in amount of titanium oxides in the products. The FESEM images of $CoTiO_3$ showed that ellipse-like grain shape particles had been achieved which had a uniform distribution with average grain size 30–50 nm. TEM image illustrated that the average diameter is 40 nm which confirmed FESEM result. By the aid of HRTEM image, it can be stated that $CoTiO_3$ has clear lattice fringes which are measured as about 0.357. For more clarifying the effect of the chelate agent, XRD comparison of powders prepared in presence and absence of EDTA was performed. Based on this comparison, it has been shown that impurities such asCoO, Co_3O_4, and Co_2TiO_4 were present in the final product. On the other hand, due to this fact that EDTA provide a proper configuration for bonding to coordinate as a bidentate, impurities have been eliminated in the presence of EDTA. Furthermore, not only EDTA specifically controlled the atomic ratio of O, Co, and Ti in the precursor, but also declined the distance among individual atoms, so that nano sized and pure $CoTiO_3$ could be achieved. In this study, three possible steps have been proposed in order to clarify the formation of $CoTiO_3$ which be discussed in the following. The first step is hydrolysis and polycondensation of tetra butyl orthotitanate. Due to the tendency of $Ti(OC_4H_9)_4$ to hydrolyze and condensate in aqueous solution, polycondensation process will occur which leads to the formation of branched oligomers and polymers with a metal oxo-based skeleton and reactive residual hydroxo and alkoxy groups. Scheme 4 (section 1–3) indicates the hydrolysis and condensation processes of $Ti(OC_4H_9)_4$.

The second step is chelation where in free Co^{2+} was trapped by chelate agent in the condensation nets in the $[-Ti-O-]_n$ gel structure. Based on the pH value which alters the microstructure of the polymer, two situations could occur. The first one is that acidic condition led to produce partially hydrolyzed monomers which condense into a more linear, lightly cross linked network (nominated as polymer I) [46]. The second one is that a neutral condition led to increasing the condensation rate and as a consequence, polymer grew progressively and deeply crosslinked network structure obtained (nominated as polymer II). Scheme 4 (sections 4–6) shows the corresponding formulas. The activity of hydrolysis condensation of the Ti-alkoxide is controlled and the sol becomes stable and difficult to gelatinize if $Ti(OR)_n$ chelated by EDTA for a desirable condition (pH at 2.0–4.0). On the other hand, when the condensation polymer grows progressively, the Co element segregates from the Ti element and all the metal atoms cannot distribute each other homogeneously after pyrolysis. Hence, uniform $CoTiO_3$ nanocrystallites formation is not out of mind. The third step is the formation of $CoTiO_3$ by calcinations. In order to network polymer converts to final products drying and pyrolysis of organics, structural rearrangement, densification, and crystallization must occur [110]. The calcination temperature and the pyrolysis condition altered the producing phase. By increasing the calcining temperature, the polymer I firstly decomposed Co_3O_4 from 400 to 500 and TiO_2 from 500 to 600 °C, then the two oxides were synthesized into $CoTiO_3$ at 700 °C. At higher temperature Co_2TiO_4 phase

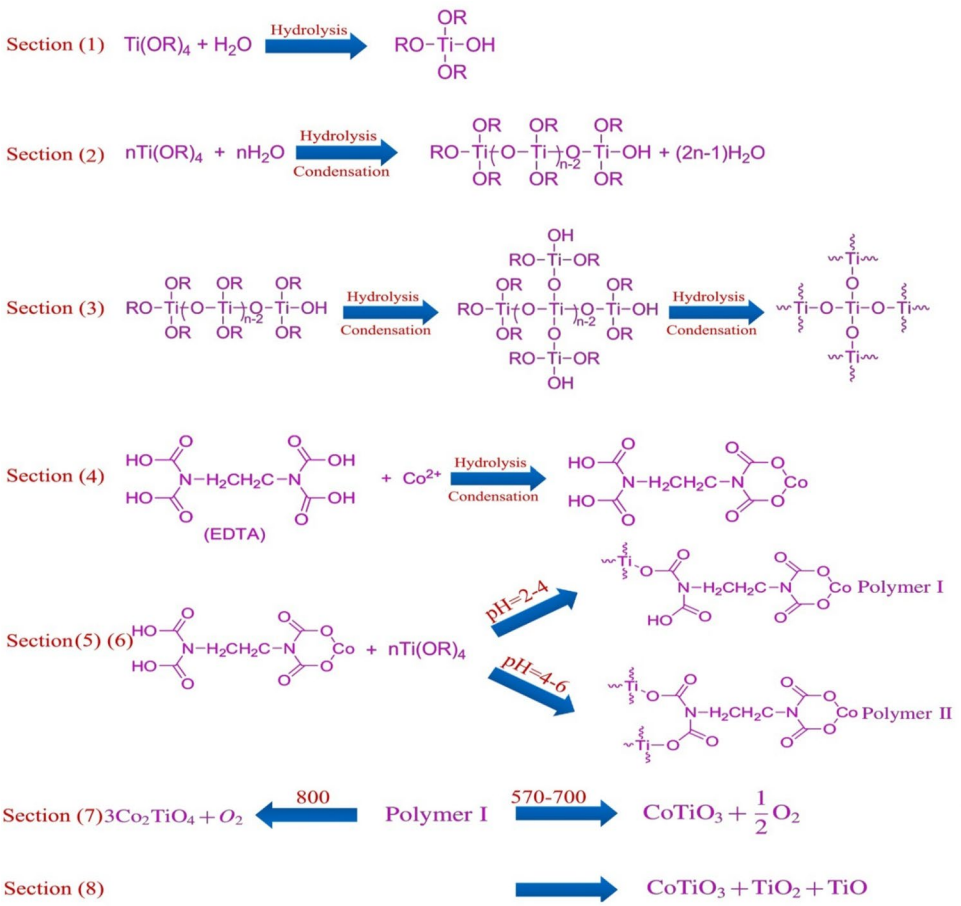

Scheme 4 Schematic mechanism for the synthesis of $CoTiO_3$ different pH

can be formed. As for polymer II, owing to the progressively condensed structure it decomposed much more titanium oxides. Hence, further unwanted phases were achieved in the products. Scheme 4 (Sections 10–10) describes the formation of $CoTiO_3$ and decomposition of gels.

Finally, in this study [43] it has been demonstrated that the sensor based on as-prepared $CoTiO_3$ showed good sensitivity to 104 ppm ethanol which its results come as follow:

Table 3 Selected approaches for synthesis of $CoTiO_3$ nanopaerticles and their applications

Synthesis method	Band gap (eV)	Precursor(s)	Average size (nm)	Property	Ref
Sol–gel	1.7 and 2.3	$CoCl_2{\cdot}6H_2O$ and $Ti[OCH(CH_3)_2]_4$	75 nm	Photocatalytic	[112]
Hydrothermal	2.6	$Co(CH_3COO)_2{\cdot}4H_2O$ and $Ti(OCH(CH_3)_2)$	15 nm	Photocatalytic	[113]
Solid state	–	Titanium dioxide and Cobalt oxide	8–10 nm	Dielectric	[114]
Precipitation deposition	2.4	$Ti(OC_4H_9)_4$ and $Co(CH_3COO)_2{\cdot}4H_2O$	300–700 nm	Photocatalytic	[115]
Sputtering	–	$Co(NO_3)_2{\cdot}6H_2O$ and $Ti(OC_4H_9)_4$	Thickness 12.67 nm	Humidity sensing	[116]
Sol–gel electrospinning	–	Ti $(OC4H_9)_4$ and $Co(CH_3COO)_2{\cdot}2H_2O$	220 nm	–	[87]
Solid state	–	Cobalt nitrate hexahydrate and Titaniume dioxide	50 and 100 nm	Adsorption	[117]
Pechini	2.43	Nickel acetate and Titanium *n*-butoxide	20–200 nm	Optical	[94]
Coprecipitation	2.28	Titanium tetraisopropoxide and Cobalt (II) chloride hexahydrate	54	Photocatalytic	[118]
Sol–gel	2.036 and 2.94	Titanium isopropoxide and Cobalt nitrate	100 nm	Catalytic	[119]
Hyydrothermal		TiO_2 and $CoCl_2{\cdot}6H2O$	400 to 500 nm	Catalyst	[120]
Sol–gel	–	$CoCl_2(H_2O)_6$, and $Ti[O(CH_2)_3CH_3]_4$	10–50 nm	Electrocatalytic	[121]
Sol–gel	–	$Co(NO_3)_2{\cdot}6H_2O$ and $Ti(OC_4H_9)_4$	100 nm	Sensor	[122]

response value $S = 17.9$, response time = 13 s, and recovery time = 10 s. Table 3 shows a summary of the various of synthesis method and precursors applied in the preparation of $CoTiO_3$ nanoparticles.

Rasalingam et al. [111] worked on the influence of humidity on the phase composition of $CoTiO_3$ perovskites which were prepared by a modified Pechini method. It has been demonstrated that the structural composition of the obtained materials could be changed due to altering the coordination and/or oxidation state of the Co^{2+} in the precursor solution. Thus, to clarify this impact of humidity, UV–Vis spectroscopic analysis at various humidity values had performed. It is well-known that owing to the formation of $\left[Co\left(H_2O\right)_6\right]^{2+}$, the pale pink is the color of aqueous solution of $Co(NO_3)_2$. It has been revealed that at lower humidity a bluish-pink precursor solution obtained whereas its color changed to orange-pink at high humidity which in this condition a peak with an absorbance maximum (λ_{max}) at 511 nm was observed. Therefore, the following electronic transitions can be mentioned: $^4T_{1g}$ to $^4T_{2g}$, $^4T_{1g}$ to $^4A_{2g}$ and $^4T_{1g}(F)$ to $^4T_{2g}(P)$. Furthermore, λ_{max} shifts slightly to 519 nm at lower humidity condition. Moreover, it has been stated in this investigation that the amount of $CoTiO_3$ present in the composite material has a vital role in the variation of the amount of oxygen evolved.

Similar to $MnTiO_3$ and $FeTiO_3$ in the case of $CoTiO_3$, a review of various published papers shows that the best synthesis method for achieving a high purity structure with suitable physical properties is the sol–gel method. $CoTiO_3$ can be synthesized in different sizes using this method by adjusting the effective parameters in the synthesis. Synthesis in different sizes is certainly important for the use of this compound in different applications and this adjustability has made the sol gel method a powerful method for the synthesis of such titanates.

5 Outcome

Different chemical methods for preparation of metal titanate were investigated.

The sol–gel method is a common procedure for the fabrication of metal titanate.

The sol–gel method led to preparation of nanoparticles with uniform size distribution.

One can control pH, time, temperature reaction, surfactant, M^{2+} and Ti^{4+} sources with the help of sol–gel method.

$MnTiO_3$, $FeTiO_3$, and $CoTiO_3$ nanoparticles could be used as pigment for various applications.

Metal titanate nanoparticles have pervoskite structures. The metal titanate has different properties such as optical, magnetic, and photocatalytic electrochemical.

References

1. M. Rahimi-Nasrabadi, M. Behpour, A. Sobhani-Nasab, S.M. Hosseinpour-Mashkani, $ZnFe_{2-x}La_xO_4$ nanostructure: synthesis, characterization, and its magnetic properties. J. Mater. Sci.: Mater. Electron. **26**(12), 9776–9781 (2015)
2. M. Rahimi-Nasrabadi, M. Behpour, A. Sobhani-Nasab, M.R. Jeddy, Nanocrystalline Ce-doped copper ferrite: synthesis, characterization, and its photocatalyst application. J. Mater. Sci.: Mater. Electron. **27**(11), 11691–11697 (2016)
3. R. Padash, A. Sobhani-Nasab, M. Rahimi-Nasrabadi, M. Mirmotahari, H. Ehrlich, A. Rad et al., Is it possible to use X 12 Y 12 (X = Al, B, and Y = N, P) nanocages for drug-delivery systems? A DFT study on the adsorption property of 4-aminopyridine drug. Appl. Phys. A **124**(9), 582 (2018)
4. H.R. Naderi, A. Sobhani-Nasab, M. Rahimi-Nasrabadi, M.R. Ganjali, Decoration of nitrogen-doped reduced graphene oxide with cobalt tungstate nanoparticles for use in high-performance supercapacitors. Appl. Surf. Sci. **423**, 1025–1034 (2017)
5. M. Eghbali-Arani, A. Sobhani-Nasab, M. Rahimi-Nasrabadi, F. Ahmadi, S. Pourmasoud, Ultrasound-assisted synthesis of YbVO4 nanostructure and $YbVO_4/CuWO_4$ nanocomposites for enhanced photocatalytic degradation of organic dyes under visible light. Ultrason. Sonochem. **43**, 120–135 (2018)
6. A. Sobhani-Nasab, A. Ziarati, M. Rahimi-Nasrabadi, M.R. Ganjali, A. Badiei, Five-component domino synthesis of tetrahydropyridines using hexagonal $PbCr_xFe_{12-x}O_{19}$ as efficient magnetic nanocatalyst. Res. Chem. Intermed. **43**(11), 6155–6165 (2017)
7. S. Pourmasoud, A. Sobhani-Nasab, M. Behpour, M. Rahimi-Nasrabadi, F. Ahmadi, Investigation of optical properties and the photocatalytic activity of synthesized $YbYO_4$ nanoparticles and $YbVO_4/NiWO_4$ nanocomposites by polymeric capping agents. J. Mol. Struct. **1157**, 607–615 (2018)
8. J. Amani, M. Maleki, A. Khoshroo, A. Sobhani-Nasab, M. Rahimi-Nasrabadi, An electrochemical immunosensor based on poly p-phenylenediamine and graphene nanocomposite for detection of neuron-specific enolase via electrochemically amplified detection. Anal. Biochem. **548**, 53–59 (2018)
9. M. Eghbali-Arani, A. Sobhani-Nasab, M. Rahimi-Nasrabadi, S. Pourmasoud, Green synthesis and characterization of $SmVO_4$ nanoparticles in the presence of carbohydrates as capping agents with investigation of visible-light photocatalytic properties. J. Electron. Mater. **47**, 3757–3769 (2018)
10. A. Sobhani-Nasab, S. Pourmasoud, F. Ahmadi, M. Wysokowski, T. Jesionowski, H. Ehrlich et al., Synthesis and characterization of $MnWO_4/TmVO_4$ ternary nano-hybrids by an ultrasonic method for enhanced photocatalytic activity in the degradation of organic dyes. Mater. Lett. **238**, 159–162 (2019)
11. F. Sedighi, M. Esmaeili-Zare, A. Sobhani-Nasab, M. Behpour, Synthesis and characterization of $CuWO_4$ nanoparticle and $CuWO_4$/NiO nanocomposite using co-precipitation method; application in photodegradation of organic dye in water. J. Mater. Sci.: Mater. Electron. **29**(16), 13737–13745 (2018)
12. A. Sobhani-Nasab, M. Behpour, M. Rahimi-Nasrabadi, F. Ahmadi, S. Pourmasoud, New method for synthesis of $BaFe_{12}O_{19}/Sm_2Ti_2O_7$ and $BaFe_{12}O_{19}/Sm_2Ti_2O_7/Ag$ nanohybrid and investigation of optical and photocatalytic properties. J. Mater. Sci.: Mater. Electron. **30**(6), 5854–5865 (2019)
13. M.A. Marsooli, M. Rahimi-Nasrabadi, M. Fasihi-Ramandi, K. Adib, M. Eghbali-Arani, F. Ahmadi et al., Preparation of $Fe_3O_4/SiO_2/TiO_2/CeVO_4$ nanocomposites: investigation of photocatalytic effects on organic pollutants, bacterial environments and new potential therapeutic candidate against cancer cells. Front. Pharmacol. **11**, 192 (2020)

14. A. Sobhani-Nasab, S. Behvandi, M.A. Karimi, E. Sohouli, M.S. Karimi, N. Gholipour et al., Synergetic effect of graphene oxide and C3N4 as co-catalyst for enhanced photocatalytic performance of dyes on $Yb_2(MoO_4)_3$/$YbMoO_4$ nanocomposite. Ceram. Int. **45**(14), 17847–17858 (2019)
15. M.A. Marsooli, M. Fasihi-Ramandi, K. Adib, S. Pourmasoud, F. Ahmadi, M.R. Ganjali et al., Preparation and characterization of magnetic Fe_3O_4/$CdWO_4$ and Fe_3O_4/$CdWO_4$/$PrVO_4$ nanoparticles and investigation of their photocatalytic and anticancer properties on PANC1 cells. Materials **12**(19), 3274 (2019)
16. A. Khoshroo, L. Hosseinzadeh, A. Sobhani-Nasab, M. Rahimi-Nasrabadi, F. Ahmadi, Silver nanofibers/ionic liquid nanocomposite based electrochemical sensor for detection of clonazepam via electrochemically amplified detection. Microchem. J. **145**, 1185–1190 (2019)
17. S.M. Hosseinpour-Mashkani, M. Ramezani, A. Sobhani-Nasab, M. Esmaeili-Zare, Synthesis, characterization, and morphological control of $CaCu_3Ti_4O_{12}$ through modify sol–gel method. J. Mater. Sci.: Mater. Electron. **26**(8), 6086–6091 (2015)
18. A. Sobhani-Nasab, M. Behpour, Synthesis, characterization, and morphological control of $Eu_2Ti_2O_7$ nanoparticles through green method and its photocatalyst application. J. Mater. Sci.: Mater. Electron. **27**(11), 11946–11951 (2016)
19. S.M. Hosseinpour-Mashkani, M. Maddahfar, A. Sobhani-Nasab, Precipitation synthesis, characterization, morphological control, and photocatalyst application of $ZnWO_4$ nanoparticles. J. Electron. Mater. **45**(7), 3612–3620 (2016)
20. A. Sobhani-Nasab, M. Behpour, Synthesis and characterization of AgO nanostructures by precipitation method and its photocatalyst application. J. Mater. Sci.: Mater. Electron. **27**(2), 1191–1196 (2016)
21. A. Sobhani-Nasab, M. Rangraz-Jeddy, A. Avanes, M. Salavati-Niasari, Novel sol–gel method for synthesis of $PbTiO_3$ and its light harvesting applications. J. Mater. Sci.: Mater. Electron. **26**(12), 9552–9560 (2015)
22. M. Ramezani, A. Sobhani-Nasab, A. Davoodi, Bismuth selenide nanoparticles: simple synthesis, characterization, and its light harvesting applications in the presence of novel precursor. J. Mater. Sci.: Mater. Electron. **26**(7), 5440–5445 (2015)
23. A. Sobhani-Nasab, H. Naderi, M. Rahimi-Nasrabadi, M.R. Ganjali, Evaluation of supercapacitive behavior of samarium tungstate nanoparticles synthesized via sonochemical method. J. Mater. Sci.: Mater. Electron. **28**(12), 8588–8595 (2017)
24. S.M. Hosseinpour-Mashkani, A. Sobhani-Nasab, Green synthesis and characterization of $NaEuTi_2O_6$ nanoparticles and its photocatalyst application. J. Mater. Sci.: Mater. Electron. **28**(5), 4345–4350 (2017)
25. S.M. Hosseinpour-Mashkani, A. Sobhani-Nasab, A simple sonochemical synthesis and characterization of $CdWO_4$ nanoparticles and its photocatalytic application. J. Mater. Sci.: Mater. Electron. **27**(4), 3240–3244 (2016)
26. M. Ramezani, S.M. Hosseinpour-Mashkani, A. Sobhani-Nasab, H.G. Estarki, Synthesis, characterization, and morphological control of $ZnMoO_4$ nanostructures through precipitation method and its photocatalyst application. J. Mater. Sci.: Mater. Electron. **26**(10), 7588–7594 (2015)
27. S.M. Hosseinpour-Mashkani, A. Sobhani-Nasab, Simple synthesis and characterization of copper tungstate nanoparticles: investigation of surfactant effect and its photocatalyst application. J. Mater. Sci.: Mater. Electron. **27**(7), 7548–7553 (2016)
28. M. Ramezani, A. Sobhani-Nasab, S.M. Hosseinpour-Mashkani, Synthesis, characterization, and morphological control of $Na_{1/2}Bi_{1/2}Cu_3Ti_4O_{12}$ through modify sol–gel method. J. Mater. Sci.: Mater. Electron. **26**(7), 4848–4853 (2015)
29. A. Javidan, M. Ramezani, A. Sobhani-Nasab, S.M. Hosseinpour-Mashkani, Synthesis, characterization, and magnetic property of monoferrite $BaFe_2O_4$ nanoparticles with aid of a novel precursor. J. Mater. Sci.: Mater. Electron. **26**(6), 3813–3818 (2015)
30. S.M. Hosseinpour-Mashkani, A. Sobhani-Nasab, M. Mehrzad, Controlling the synthesis $SrMoO_4$ nanostructures and investigation its photocatalyst application. J. Mater. Sci.: Mater. Electron. **27**(6), 5758–5763 (2016)
31. M. Rahimi-Nasrabadi, A. Ghaderi, H.R. Banafshe, M. Eghbali-Arani, M. Akbari, F. Ahmadi et al., Preparation of Co_2TiO_4/$CoTiO_3$/polyaniline ternary nano-hybrids for enhanced destruction of agriculture poison and organic dyes under visible-light irradiation. J. Mater. Sci.: Mater. Electron. **30**(17), 15854–15868 (2019)
32. S.M. Asgarian, S. Pourmasoud, Z. Kargar, A. Sobhani-Nasab, M. Eghbali-Arani, Investigation of positron annihilation lifetime and magnetic properties of $Co_{1-x}Cu_xFe_2O_4$ nanoparticles. Mater. Res. Express **6**(1), 015023 (2018)
33. A. Sobhani-Nasab, M. Behpour, M. Rahimi-Nasrabadi, F. Ahmadi, S. Pourmasoud, F. Sedighi, Preparation, characterization and investigation of sonophotocatalytic activity of thulium titanate/polyaniline nanocomposites in degradation of dyes. Ultrason. Sonochem. **50**, 46–58 (2019)
34. S.M. Peymani-Motlagh, N. Moeinian, M. Rostami, M. Fasihi-Ramandi, A. Sobhani-Nasab, M. Rahimi-Nasrabadi et al., Effect of Gd3+-, Pr3+-or Sm3+-substituted cobalt–zinc ferrite on photodegradation of methyl orange and cytotoxicity tests. J. Rare Earths **37**(12), 1288–1295 (2019)
35. F. Gandomi, S.M. Peymani-Motlagh, M. Rostami, A. Sobhani-Nasab, M. Fasihi-Ramandi, M. Eghbali-Arani et al., Simple synthesis and characterization of $Li_{0.5}Fe_{2.5}O_4$, $LiMg_{0.5}Fe_2O_4$ and $LiNi_{0.5}Fe_2O_4$, and investigation of their photocatalytic and anticancer properties on hela cells line. J. Mater. Sci.: Mater. Electron. **30**(22), 19691–19702 (2019)
36. H. Kooshki, A. Sobhani-Nasab, M. Eghbali-Arani, F. Ahmadi, V. Ameri, M. Rahimi-Nasrabadi, Eco-friendly synthesis of $PbTiO_3$ nanoparticles and $PbTiO_3$/carbon quantum dots binary nanohybrids for enhanced photocatalytic performance under visible light. Sep. Purif. Technol. **211**, 873–881 (2019)
37. Z.-Q. Song, S.-B. Wang, W. Yang, M. Li, H. Wang, H. Yan, Synthesis of manganese titanate $MnTiO_3$ powders by a sol–gel–hydrothermal method. Mater. Sci. Eng. B **113**(2), 121–124 (2004)
38. J.J. Stickler, S. Kern, A. Wold, G. Heller, Magnetic resonance and susceptibility of several ilmenite powders. Phys. Rev. **164**(2), 765 (1967)
39. H. Watanabe, H. Yamauchi, H. Takei, Magnetic anisotropies in $MTiO_3$ (M= Co, Ni). J. Magn. Magn. Mater. **15**, 549–550 (1980)
40. H.-Y. He, J.-F. Huang, L.-Y. Cao, J.-P. Wu, Humidity sensitivity of $MnTiO_3$ film prepared via chemical solution deposition process. Sensors and Actuators B: Chemical. **132**(1), 5–8 (2008)
41. M. Kharkwal, S. Uma, R. Nagarajan, Use of a chelating agent for the synthesis of high surface area pyrophanite $MnTiO_3$ powders. Mater. Lett. **64**(6), 692–694 (2010)
42. N.L. Ross, J. Ko, C.T. Prewitt, A new phase transition in $MnTiO_3$: $LiNbO_3$-perovskite structure. Phys. Chem. Miner. **16**(7), 621–629 (1989)
43. P.S. Anjana, M.T. Sebastian, Synthesis, characterization, and microwave dielectric properties of $ATiO_3$ (A = Co, Mn, Ni) ceramics. J. Am. Ceram. Soc. **89**(7), 2114–2117 (2006)
44. G.W. Zhou, Y.S. Kang, Synthesis and structural properties of manganese titanate $MnTiO_3$ nanoparticle. Mater. Sci. Eng. C **24**(1–2), 71–74 (2004)
45. Y.K. Sharma, M. Kharkwal, S. Uma, R. Nagarajan, Synthesis and characterization of titanates of the formula $MTiO_3$ (M = Mn, Fe Co, Ni and Cd) by co-precipitation of mixed metal oxalates. Polyhedron **28**(3), 579–585 (2009)

46. K.-N. Bae, S.I. Noh, H.-J. Ahn, T.-Y. Seong, Effect of $MnTiO_3$ surface treatment on the performance of dye-sensitized solar cells. Mater. Lett. **96**, 67–70 (2013)
47. M. Law, L.E. Greene, J.C. Johnson, R. Saykally, P. Yang, Nanowire dye-sensitized solar cells. Nat. Mater. **4**(6), 455 (2005)
48. A. Hagfeldt, M. Graetzel, Light-induced redox reactions in nanocrystalline systems. Chem. Rev. **95**(1), 49–68 (1995)
49. J.-H. Yum, S. Nakade, D.-Y. Kim, S. Yanagida, Improved performance in dye-sensitized solar cells employing TiO_2 photoelectrodes coated with metal hydroxides. J. Phys. Chem. B **110**(7), 3215–3219 (2006)
50. D. Menzies, Q. Dai, Y.-B. Cheng, G. Simon, L. Spiccia, Improvement of the Zirconia shell in nanostructured titania core–shell working electrodes for dye-sensitized solar cells. Mater. Lett. **59**(14–15), 1893–1896 (2005)
51. E. Palomares, J.N. Clifford, S.A. Haque, T. Lutz, J.R. Durrant, Control of charge recombination dynamics in dye sensitized solar cells by the use of conformally deposited metal oxide blocking layers. J. Am. Chem. Soc. **125**(2), 475–482 (2003)
52. Y. Xu, M.A. Schoonen, The absolute energy positions of conduction and valence bands of selected semiconducting minerals. Am. Miner. **85**(3–4), 543–556 (2000)
53. D.B. Menzies, Q. Dai, L. Bourgeois, R.A. Caruso, Y.-B. Cheng, G.P. Simon et al., Modification of mesoporous TiO_2 electrodes by surface treatment with titanium (IV), indium (III) and zirconium (IV) oxide precursors: preparation, characterization and photovoltaic performance in dye-sensitized nanocrystalline solar cells. Nanotechnology. **18**(12), 125608 (2007)
54. H.S. Jung, J.-K. Lee, M. Nastasi, S.-W. Lee, J.-Y. Kim, J.-S. Park et al., Preparation of nanoporous MgO-coated TiO_2 nanoparticles and their application to the electrode of dye-sensitized solar cells. Langmuir **21**(23), 10332–10335 (2005)
55. T. Robinson, B. Chandran, P. Nigam, Removal of dyes from a synthetic textile dye effluent by biosorption on apple pomace and wheat straw. Water Res. **36**(11), 2824–2830 (2002)
56. H. He, W. Dong, G. Zhang, Photodegradation of aqueous methyl orange on $MnTiO_3$ powder at different initial pH. Res. Chem. Intermed. **36**(9), 995–1001 (2010)
57. T. Acharya, R. Choudhary, Dielectric behavior of manganese titanate in the paraelectric phase. Appl. Phys. A **121**(2), 707–714 (2015)
58. Y. Absalan, I.G. Bratchikova, N.N. Lobanov, O.V. Kovalchukova, Novel synthesis method for photo-catalytic system based on some 3d-metal titanates. J. Mater. Sci.: Mater. Electron. **28**(23), 18207–18219 (2017)
59. U. Mohanty, S. Kaushik, H. Bhatt, M. Deo, I. Naik, editors, Neutron diffraction and magnetic behavior of ilmenite $MnTiO_3$, in *AIP Conference Proceedings*, AIP Publishing LLC, 2019
60. X. Li, H. Zhang, J. Luo, Z. Feng, J. Huang, Hydrothermal synthesized novel nanoporous g-C_3N_4/$MnTiO_3$ heterojunction with direct Z-scheme mechanism. Electrochim. Acta **258**, 998–1007 (2017)
61. R. Nakhowong, Fabrication and characterization of $MnTiO_3$ nanofibers by sol–gel assisted electrospinning. Mater. Lett. **161**, 468–470 (2015)
62. W. Dong, D. Wang, L. Jiang, H. Zhu, H. Huang, J. Li et al., Synthesis of F doping $MnTiO_3$ nanodiscs and their photocatalytic property under visible light. Mater. Lett. **98**, 265–268 (2013)
63. R. Harrison, S. Redfern, Short-and long-range ordering in the ilmenite–hematite solid solution. Phys. Chem. Miner. **28**(6), 399–412 (2001)
64. X. Tang, K.-A. Hu, The formation of ilmenite $FeTiO_3$ powders by a novel liquid mix and H_2/H_2O reduction process. J. Mater. Sci. **41**(23), 8025–8028 (2006)
65. T. Fujii, M. Kayano, Y. Takada, M. Nakanishi, J. Takada, Ilmenite–hematite solid solution films for novel electronic devices. Solid State Ion. **172**(1–4), 289–292 (2004)
66. Z. Dai, P. Zhu, S. Yamamoto, A. Miyashita, K. Narum, H. Naramoto, Pulsed laser deposition of ilmenite $FeTiO_3$ epitaxial thin film onto sapphire substrate. Thin Solid Films **339**(1–2), 114–116 (1999)
67. T. Dietl, H. Ohno, Ferromagnetic III–V and II–VI semiconductors. MRS Bull. **28**(10), 714–719 (2003)
68. X.-F. Guan, J. Zheng, M.-L. Zhao, L.-P. Li, G.-S. Li, Synthesis of $FeTiO_3$ nanosheets with 0001 facets exposed: enhanced electrochemical performance and catalytic activity. RSC Adv. **3**(33), 13635–13641 (2013)
69. J. Ru, Y. Hua, C. Xu, J. Li, Y. Li, D. Wang et al., Microwave-assisted preparation of submicron-sized $FeTiO_3$ powders. Ceram. Int. **40**(5), 6799–6805 (2014)
70. Y.J. Kim, B. Gao, S.Y. Han, M.H. Jung, A.K. Chakraborty, T. Ko et al., Heterojunction of $FeTiO_3$ nanodisc and TiO_2 nanoparticle for a novel visible light photocatalyst. J. Phys. Chem. C. **113**(44), 19179–19184 (2009)
71. A.B. Gambhire, M.K. Lande, S.B. Rathod, B.R. Arbad, K.N. Vidhate, R.S. Gholap et al., Synthesis and characterization of $FeTiO_3$ ceramics. Arab. J. Chem. **9**, S429–S432 (2016)
72. P. Srinivas, A.S. Kumar, P. Babu, A.K. Bhatnagar, Synthesis and magnetic properties of Nanocrystalline $FeTiO_3$ materials. J. Supercond. Novel Magn. **31**(4), 1189–1197 (2018)
73. D. Nakatsuka, T. Fujii, M. Nakanishi, J. Takada, editors, Synthesis of Ge substituted ilmenite and their magnetic and electronic properties, in *Journal of Physics: Conference Series*, IOP Publishing, 2010
74. P. Siva, P. Prabu, M. Selvam, S. Karthik, V. Rajendran, Electrocatalytic conversion of carbon dioxide to urea on nano-$FeTiO_3$ surface. Ionics **23**(7), 1871–1878 (2017)
75. A. Raghavender, N.H. Hong, K.J. Lee, M.-H. Jung, Z. Skoko, M. Vasilevskiy et al., Nano-ilmenite $FeTiO_3$: synthesis and characterization. J. Magn. Magn. Mater. **331**, 129–132 (2013)
76. D. Gu, Y. Qin, Y. Wen, L. Qin, H.J. Seo, Photochemical and magnetic activities of $FeTiO_3$ nanoparticles by electro-spinning synthesis. J. Taiwan Inst. Chem. Eng. **78**, 431–437 (2017)
77. A. Pataquiva-Mateus, H. Zea, J. Ramirez, Degradation of Orange II by Fenton reaction using ilmenite as catalyst. Environ. Sci. Pollut. Res. **24**(7), 6187–6194 (2017)
78. Q.D. Truong, J.-Y. Liu, C.-C. Chung, Y.-C. Ling, Photocatalytic reduction of CO_2 on $FeTiO_3/TiO_2$ photocatalyst. Catal. Commun. **19**, 85–89 (2012)
79. F. Zhang, Y. Chen, Q. Tian, Preparation of an improved performance $FeTiO_3$-based lithium-ion battery anode. Synth. Met. **260**, 116302 (2020)
80. T. Aparna, R. Sivasubramanian, $FeTiO_3$ nanohexagons based electrochemical sensor for the detection of dopamine in presence of uric acid. Mater. Chem. Phys. **233**, 319–328 (2019)
81. M. Abdou, M. Ayad, A. Diab, I. Hassan, A. Fadl, Studying the corrosion mitigation behavior and chemical durability of $FeTiO_3$/melamine formaldehyde epoxy composite coating for steel internal lining applications. Prog. Org. Coat. **133**, 325–339 (2019)
82. M. Abdou, A. Fadl, Assessment of nano-$FeTiO_3$/non crystalline silica cold galvanizing composite coating as a duplex corrosion guard system for steel electricity transmission towers in severe aggressive media. Constr. Build. Mater. **223**, 705–723 (2019)
83. S. Zhang, Y. Ruan, C. Liu, P. Wang, Y. Ma, The evolution of structure, chemical state and photocatalytic performance of α-Fe/$FeTiO_3/TiO_2$ with the nitridation at different temperatures. Mater. Res. Bull. **95**, 503–508 (2017)
84. K. Vamsi, M. Krishnakumar, R. Saravanan, Effect of preheating temperatures on distribution of FeTiO3 on A 360 aluminium alloy by stirring, in *Materials Today: Proceedings*, 2019

85. J. Jiang, J. Luo, J. Zhu, X. Huang, J. Liu, T. Yu, Diffusion-controlled evolution of core–shell nanowire arrays into integrated hybrid nanotube arrays for Li-ion batteries. Nanoscale. **5**(17), 8105–8113 (2013)
86. M. Enhessari, A. Parviz, K. Ozaee, E. Karamali, Magnetic properties and heat capacity of $CoTiO_3$ nanopowders prepared by stearic acid gel method. J. Exp. Nanosci. **5**(1), 61–68 (2010)
87. G. Yang, W. Yan, J. Wang, H. Yang, Fabrication and characterization of $CoTiO_3$ nanofibers by sol–gel assisted electrospinning. Mater. Lett. **122**, 117–120 (2014)
88. Y. Qu, W. Zhou, H. Fu, Porous cobalt titanate nanorod: a new candidate for visible light-driven photocatalytic water oxidation. ChemCatChem. **6**(1), 265–270 (2014)
89. A. Agafonov, A. Vinogradov, Catalytically active materials based on titanium dioxide: ways of enhancement of photocatalytic activity. High Energy Chem. **42**(7), 578–580 (2008)
90. M. Siemons, U. Simon, Gas sensing properties of volume-doped $CoTiO_3$ synthesized via polyol method. Sensors and Actuators B: Chemical. **126**(2), 595–603 (2007)
91. M.A. Ehsan, R. Naeem, V. McKee, A. Rehman, A.S. Hakeem, M. Mazhar, Fabrication of photoactive $CaTiO_3$–TiO_2 composite thin film electrodes via facile single step aerosol assisted chemical vapor deposition route. J. Mater. Sci.: Mater. Electron. **30**(2), 1411–1424 (2019)
92. G.W. Zhou, D.-G. Lee, Y.-H. Kim, C.-W. Kim, Y.-S. Kang, Preparation and spectroscopic characterization of ilmenite-type $ $CoTiO_3$ $ nanoparticles. Bull. Korean Chem. Soc. **27**(3), 368–372 (2006)
93. P. Kapoor, S. Uma, S. Rodriguez, K. Klabunde, Aerogel processing of MTi_2O_5 (M = Mg, Mn, Fe Co, Zn, Sn) compositions using single source precursors: synthesis, characterization and photocatalytic behavior. J. Mol. Catal. A: Chem. **229**(1–2), 145–150 (2005)
94. Y.-J. Lin, Y.-H. Chang, W.-D. Yang, B.-S. Tsai, Synthesis and characterization of ilmenite $NiTiO_3$ and $CoTiO_3$ prepared by a modified Pechini method. J. Non-Cryst. Solids **352**(8), 789–794 (2006)
95. S. Yin, D. Chen, W. Tang, Y. Peng, Synthesis of $CaTiO_3$: Pr persistent phosphors by a modified solid-state reaction. Mater. Sci. Eng., B **136**(2–3), 193–196 (2007)
96. K.S. Suslick, The chemical effects of ultrasound. Sci. Am. **260**(2), 80–86 (1989)
97. F.M. Nowak, *Sonochemistry: Theory, Reactions, Syntheses, and Applications* (Nova Science Publishers, Hauppauge, 2010)
98. G. Cravotto, P. Cintas, Power ultrasound in organic synthesis: moving cavitational chemistry from academia to innovative and large-scale applications. Chem. Soc. Rev. **35**(2), 180–196 (2006)
99. A. Moghtada, A. Shahrouzianfar, R. Ashiri, Low-temperature ultrasound synthesis of nanocrystals $CoTiO_3$ without a calcination step: effect of ultrasonic waves on formation of the crystal growth mechanism. Adv. Powder Technol. **28**(4), 1109–1117 (2017)
100. A. Agui, M. Mizumaki, Intermetallic charge transfer and band gap of $MTiO_3$ (M = Mn, Fe Co, and Ni) studied by O 1s-edge X-ray emission spectroscopy. J. Electron Spectrosc. Relat. Phenom. **184**(8–10), 463–467 (2011)
101. A. Abedini, S. Khademolhoseini, Cobalt titanate nanoparticles: synthesis, characterization, optical and photocatalytic properties. J. Mater. Sci.: Mater. Electron. **27**(1), 330–334 (2016)
102. A.H. Kianfar, P. Dehghani, M.M. Momeni, Photo-catalytic degradation of methylene blue over nano titanium/nickel oxide prepared from supported Schiff base complex on titanium dioxide. J. Mater. Sci.: Mater. Electron. **27**(4), 3368–3375 (2016)
103. M.H. Habibi, M. Fakhrpor, Improved photo-catalytic activity of novel nano-dimension Ce/Zn composite oxides deposited on flat-glass surface for removal of Acid Black 4BN dye pollution. J. Mater. Sci.: Mater. Electron. **28**(3), 2697–2704 (2017)
104. Y. Ghayeb, M.M. Momeni, Iron decorated tungsten-titania nanotubes as highly efficient photocatalysts for removal of Rhodamine B dye. J. Mater. Sci.: Mater. Electron. **27**(6), 6305–6312 (2016)
105. R. Singh, S.G. Kulkarni, Nanocomposites based on transition metal oxides in polyvinyl alcohol for EMI shielding application. Polym. Bull. **71**(2), 497–513 (2014)
106. M.H. Habibi, E. Shojaee, Complete photocatalytic mineralization of Nile blue on hetero-structured $CoTiO_3$ nano-composite coated on glass in a sol–gel process using diethylene glycol as stabilizer: effect of charge separation and calcination temperature on activity. J. Mater. Sci.: Mater. Electron. **28**(8), 5971–5978 (2017)
107. M. Siemons, U. Simon, Preparation and gas sensing properties of nanocrystalline La-doped $CoTiO_3$. Sens. Actuators B: Chem. **120**(1), 110–118 (2006)
108. J. Lu, Y. Jiang, Y. Zhang, J. Huang, Z. Xu, Preparation of gas sensing $CoTiO_3$ nanocrystallites using EDTA as the chelating agent in a sol–gel process. Ceram. Int. **41**(3), 3714–3721 (2015)
109. M.K. Yadav, A.V. Kothari, V.K. Gupta, Preparation and characterization of bi-and trimetallic titanium based oxides. Dyes Pigm. **89**(2), 149–154 (2011)
110. S. Sakka, H. Kozuka, *Handbook of Sol-Gel Science and Technology. 1. Sol-Gel Processing* (Springer, Berlin, 2005)
111. S. Rasalingam, R.T. Koodali, Visible-light driven oxygen evolution over $CoTiO_3$ perovskites via a modified Pechini method: impact of humidity on their phase composition. CrystEngComm **18**(6), 868–871 (2016)
112. M.H. Habibi, E. Shojaee, Ilmenite type nano-crystalline Co–Ti–O ternary oxides: sol–gel thin film on borosilicate glass, characterization and photocatalytic activity in mineralization of reactive red 198. J. Mater. Sci.: Mater. Electron. **28**(11), 8286–8293 (2017)
113. K. Wangkawong, S. Phanichphant, D. Tantraviwat, B. Inceesungvorn, $CoTiO_3$/Ag_3VO_4 composite: a study on the role of $CoTiO_3$ and the active species in the photocatalytic degradation of methylene blue. J. Colloid Interface Sci. **454**, 210–215 (2015)
114. T. Acharya, R. Choudhary, Structural, dielectric and impedance characteristics of $CoTiO_3$. Mater. Chem. Phys. **177**, 131–139 (2016)
115. W. Mao, K. Bao, F. Cao, B. Chen, G. Liu, W. Wang et al., Synthesis of a $CoTiO_3$/BiOBr heterojunction composite with enhanced photocatalytic performance. Ceram. Int. **43**(3), 3363–3368 (2017)
116. J. Lu, L. Cheng, Y. Zhang, J. Huang, C. Li, Effect of the seed layer on surface morphology and humidity sensing property of $CoTiO_3$ nanocrystalline film. Ceram. Int. **43**(7), 5823–5827 (2017)
117. S. Hashemian, A. Foroghimoqhadam, Effect of copper doping on $CoTiO_3$ ilmenite type nanoparticles for removal of congo red from aqueous solution. Chem. Eng. J. **235**, 299–306 (2014)
118. M.H. Habibi, E. Shojaee, Synthesis of a heterojunction $CoTiO_3$/Co_3O_4 nano-composite thin film with superior photocatalytic activity and reusability: Effect of calcination temperature on phase transformation and effect of oxidants on enhanced degradation of Indo Light Blue dye. Spectrochim. Acta Part A Mol. Biomol. Spectrosc. **229**, 117796 (2020)
119. M. Singh, F. Qin, O.I.P. Ordoñez, W. Yang, J. Bao, A. Genc et al., Unusual catalytic activity of TiO_2–$CoTiO_3$ under 1064 nm pulsed laser illumination. Catal Today (2019). https://doi.org/10.1016/j.cattod.2019.06.081
120. H. Li, Q. Gao, G. Wang, B. Han, K. Xia, C. Zhou, Architecturing $CoTiO_3$ overlayer on nanosheets-assembled hierarchical TiO_2 nanospheres as a highly active and robust catalyst for peroxymonosulfate activation and metronidazole degradation. Chem. Eng. J. (2019). https://doi.org/10.1016/j.cej.2019.123819

121. J.M. Luque-Centeno, M. Martínez-Huerta, D. Sebastián, J.I. Pardo, M. Lázaro, $CoTiO_3$/NrGO nanocomposites for oxygen evolution and oxygen reduction reactions: synthesis and electrocatalytic performance. Electrochim. Acta **331**, 135396 (2020)
122. J. Lu, N. Jia, L. Cheng, K. Liang, J. Huang, J. Li, rGO/$CoTiO_3$ nanocomposite with enhanced gas sensing performance at low working temperature. J. Alloy. Compd. **739**, 227–234 (2018)